Phase composition of iron oxide nanoparticles studied using hard X-ray absorption spectroscopy

Xiao Sun, Akhil Tayal, Aladin Ullrich, Oleg Petracic, Sylvio Haas

Angaben zur Veröffentlichung / Publication details:

Sun, Xiao, Akhil Tayal, Aladin Ullrich, Oleg Petracic, and Sylvio Haas. 2023. "Phase composition of iron oxide nanoparticles studied using hard X-ray absorption spectroscopy." *The Journal of Physical Chemistry C* 127 (25): 12077–83. https://doi.org/10.1021/acs.jpcc.3c01023.

THE JOURNAL OF PHYSICAL CHEMISTRY C
A JOURNAL OF THE AMERICAN CHEMICAL SOCIETY

pubs.acs.org/JPCC

Article

Phase Composition of Iron Oxide Nanoparticles Studied Using Hard X-ray Absorption Spectroscopy

Xiao Sun,* Akhil Tayal, Aladin Ullrich, Oleg Petracic, and Sylvio Haas

Cite This: *J. Phys. Chem. C* 2023, 127, 12077−12083

Read Online

ACCESS | Metrics & More | Article Recommendations | Supporting Information

ABSTRACT: At the surface of iron oxide nanoparticles, an oxidized or disordered layer is often found. Due to the large surface-to-volume ratio of nanomaterials, such a surface layer plays an important role in the overall magnetic properties of the particles. Consequently, it is important to characterize the surface layer if applications of iron oxide nanoparticles, e.g., for magnetic hyperthermia, magnetic particle imaging, or ferrofluidics, are envisaged. In this work, we tuned the phase of the surface layer of 14 nm iron oxide nanoparticles via annealing procedures. The phase composition of the particles is systematically studied using hard X-ray absorption spectroscopy.

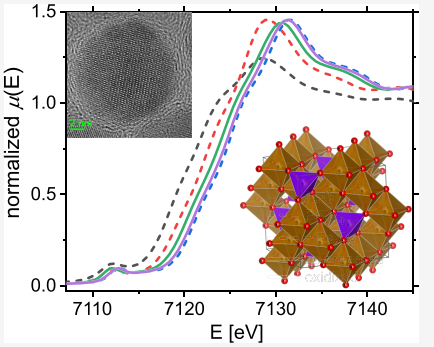

1. INTRODUCTION

Magnetic iron oxide nanoparticles (NPs) are in the focus of intense research activities because of their existing and potential use in nanomedical and ferrofluidic applications.[1−13] To synthesize iron oxide particles with the desired properties, the exact relationship between their magnetic properties and their crystallographic structure and phase composition needs to be understood. In this work, we specifically focus on systematic hard X-ray absorption spectroscopy (XAS) investigations to characterize the phase composition inside the particles.

Depending on their crystallographic structure and their oxidation state, iron oxides show different magnetic properties. FeO (wüstite) containing purely divalent Fe^{2+} is an antiferromagnet (AF) with a rock salt crystallographic structure.[14−17] Its AF to paramagnetic (PM) phase transition is found at 198 K in bulk. With increasing oxygen content, FeO can be transformed via a topotactic phase transition to Fe_3O_4 (magnetite). Here, two-thirds of the Fe^{2+} is oxidized to Fe^{3+}. Fe_3O_4 is a ferrimagnet (FiM) with a Curie temperature of 858 K in bulk and has an inverse spinel crystal structure, $(8Fe^{3+})_A[8Fe^{2+} + 8Fe^{3+}]_B\ 32O^{2-}$.[14,16] One-half of the Fe^{3+} ions occupy tetrahedral A sites. The other half together with the Fe^{2+} ions occupy the octahedral B sites. In addition, Fe_3O_4 displays a metal-to-insulator transition at the so-called Verwey transition at 125 K in bulk.[18−20] When Fe_3O_4 is further oxygenated, γ-Fe_2O_3 (maghemite) is obtained, which has a similar inverse spinel structure as Fe_3O_4. Its crystal structure can be considered as a magnetite structure but with 8/3 cation vacancies at the octahedral sites, $(8Fe^{3+})_A[40/3Fe^{3+} + 8/3\square]_B\ 32O^{2-}$. Below its Curie temperature of 948 K, γ-Fe_2O_3 transforms from PM to FiM.[14,16] The transition temperatures in NP systems are usually reduced compared to their bulk values due to the finite size effect.[11,21−27]

XAS techniques have been widely used to study the oxidation state and the local structures of iron-containing minerals.[28−38] By analyzing the extended X-ray absorption fine structure (EXAFS) spectra, information about the local structure is obtained and compared with theoretical calculations.[28] A clear chemical shift is found in the X-ray absorption near-edge structure (XANES) region, characterizing the change of the oxidation state of Fe ions.[28,29,32,34] Furthermore, the pre-edge features provide additional information about the oxidation states and local coordination environment of the Fe ions.[31,36,37,39−41]

2. EXPERIMENTAL SECTION

Spherical iron oxide NPs were synthesized based on the procedure described in ref 42 with a few modifications (Supporting Information). Magnetic properties of the NPs were characterized using a PPMS (Physical Property Measurement System) from Quantum Design with the Vibrating Sample Magnetometer (VSM) option. For the magnetometry measurements, the NP dispersion was drop-casted on a piece of silicon substrate (5 mm × 5 mm). The total magnetic moment of the sample was measured with the substrate

Received: February 14, 2023
Revised: May 23, 2023
Published: June 13, 2023

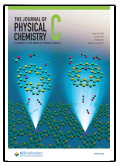

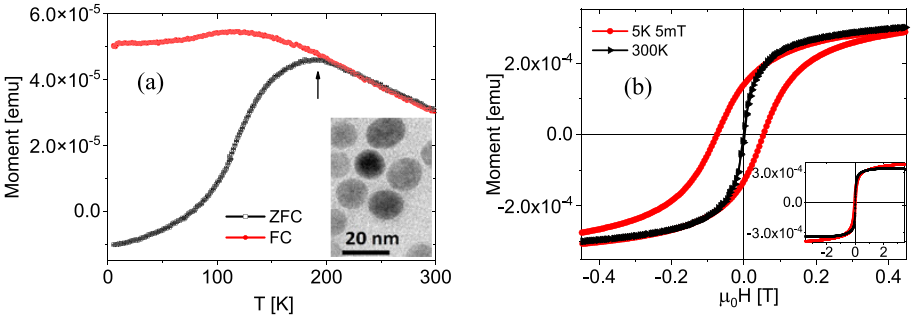

Figure 1. (a) ZFC/FC magnetization curves of spherical iron oxide NPs with a 14 nm diameter measured at 5 mT. Inset in (a) shows a TEM image of the particles. (b) Hysteresis loops of the as-prepared iron oxide NPs measured at 300 and 5 K after field cooling in 5 mT.

oriented in-plane to the applied magnetic field. Temperature-dependent magnetization curves were measured with two procedures. After the sample was cooled in zero magnetic field from room temperature to 5 K, an external magnetic field of 5 mT was applied. The zero-field cooled (ZFC) magnetization curve was then recorded during warming in the applied field. After the temperature reached 300 K, the field-cooled (FC) magnetization curve was measured during cooling to 5 K in the same magnetic field. Field-dependent magnetization curves were measured both at 300 and 5 K after the sample was cooled at an applied magnetic field of 5 mT. The magnetization curves were measured during changing the magnetic field from +9 to − 9 T and then back to +9 T.

The morphology of the NPs was characterized by transmission electron microscopy (TEM) and small-angle X-ray scattering (SAXS). The SAXS patterns were collected at the P08 beamline at PETRA III, DESY, using a PerkinElmer detector. XAS measurements around the Fe K-edge (7112 eV) were performed at the P65 beamlines at PETRA III, DESY, using a Si(111) double-crystal monochromator. For both SAXS and XAS measurements, the NP dispersions were drop-casted onto a piece of Kapton foil. The samples were measured in transmission mode for SAXS. The sample was hereby placed with the substrate plane perpendicular to the beam. For the XAS measurements, the sample was mounted 45° to the incoming X-ray beam. The XAS pattern was measured simultaneously in both the transmission and fluorescence modes. An ionic chamber was placed before the sample position to obtain the monitor signal, and a second ionic chamber was placed after the sample position to obtain the absorption signal of the sample in transmission geometry. An additional passivated implanted planar silicon (PIPS) detector was mounted 45° to the beam and 90° to the sample for simultaneous fluorescence measurements. Compared to the data measured in the transmission mode, the XAS data measured in the fluorescence mode has much higher quality. This is because the drop-casting method used to prepare the samples results in an uncontrollable and inhomogeneous sample thickness, which affects the transmission measurement. Therefore, the XAS data shown in this work were measured in the fluorescence mode.

3. RESULTS AND DISCUSSION

The size and the shape of the as-prepared NPs were characterized using TEM (Figure 1a, inset) and SAXS. Both results show that the particles are spherical with a mean diameter of 14.4 nm. The polydispersity of the size distribution obtained from the SAXS pattern is 22.1% (Supporting Information Figure S1).

Figure 1a shows the ZFC/FC magnetization curves of the 14 nm iron oxide NPs. The ZFC curve shows a maximum at 200 ± 10 K, below which the ZFC and FC curves split. Such behavior is often observed in non-interacting superparamagnetic systems or interacting, e.g., super-spin, glass systems.[11,24,43−47] Moreover, the FC curve displays a weak step-like feature at around 120 K, which matches the Verwey transition temperature of magnetite, while in the ZFC curve, this feature is masked by the larger slope at this temperature in comparison to the FC curve. Another explanation for a decrease of the FC curve is the presence of inter-NP interactions.[43] Here, it is very likely that both effects play a role, i.e., a small fraction of magnetite in the NPs is present, and that non-negligible inter-particle interactions also occur. The latter is expected due to the close packing of NPs in the drop-casted sample morphology and, hence, significant magnetic dipolar interactions.[48] Since the ratio of magnetite is small, we conclude that the as-prepared NPs are composed of mainly maghemite with a small fraction of magnetite. Even though there is no clear evidence indicating the presence of FeO, the existence of a small amount of FeO cannot be excluded. This will be discussed later below.

Furthermore, the field-dependent magnetization curve shows an open hysteresis loop at 5 K after cooling in a magnetic field of 5 mT, while at 300 K, a closed paramagnetic-like loop shape is encountered (Figure 1b). Such a behavior is expected for superparamagnetic systems, i.e., superparamagnetic-blocked behavior with an open hysteresis loop well below the blocking temperature and unblocked behavior well above the blocking temperature.[45,47,49−51] In the low-temperature M(H) curve, one also finds that the center of the hysteresis loop is shifted by about 11.2 mT toward the negative direction. Obviously an exchange-bias (EB) effect[52−62] is found. EB is often a characteristic feature of heterosystems composed of an AF and a ferromagnet (FM), where the AF material exhibits a unidirectional bias of the FM hysteresis loop. EB effects have also been reported for the AF−FiM, FM−FiM, and FiM−FiM heterosystems or core-shell particles where the shell is composed of disordered spins or form a spin-glass like layer.[18,22,45−54] In this case, the EB interaction occurs at the interface between the two different FiM components, i.e., magnetite and maghemite, inside the NPs.

To investigate how the exchange interactions between different phases influence the overall magnetic properties of iron oxide NPs, both the temperature- and field-dependent

https://doi.org/10.1021/acs.jpcc.3c01023
J. Phys. Chem. C 2023, 127, 12077−12083

magnetization curves were measured after the as-prepared sample was oxidized in air at 50 °C for 24 h (Supporting Information Figure S5). Both the ZFC/FC curves and the hysteresis loops show similar behavior as that of the as-prepared samples. However, the peak temperature in the ZFC curve shifts from about 200 to 160 K. Moreover, the FC curve does not show a decrease below the peak temperature. This indicates that the ratio of magnetite and/or wüstite is reduced. The exchange interactions at the interface between the different phases stabilize the FiM spins of maghemite, thus resulting in a higher peak temperature in the ZFC curve of the as-prepared sample. After oxidation, the exchange interaction is much weaker due to the reduced amount of magnetite or wüstite. Thus, the peak temperature is found to be lower. Furthermore, the coercive field in the hysteresis loop of the oxidized sample is smaller compared to that of the as-prepared NPs due to the weaker effective magnetic anisotropy.

For well-controlled technological applications of the iron oxide NPs, their internal composition needs to be thoroughly characterized. In this work, we focus on hard X-ray absorption spectroscopy studies at the Fe K-edge. It is well-known that in particular, XANES is sensitive to the valence states of atoms in the materials. Compared to metallic Fe, the absorption edge of Fe^{2+} is reported to be shifted toward higher energies by a few eV. For Fe^{3+}, the XANES profile is further shifted.[28,32,35,63−67] Such chemical shifts are also found in the XANES spectra of our reference samples FeO, Fe_3O_4, and γ-Fe_2O_3, as can be seen in Figure 2a. The maximum and half-maximum positions of the

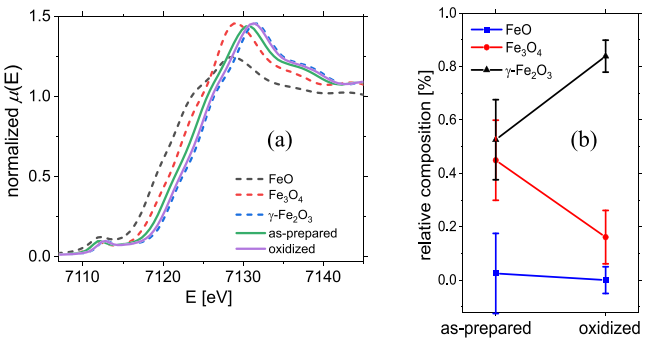

Figure 2. (a) Comparison of the Fe K-edge XANES spectra of 14 nm iron oxide NPs with reference systems. (b) Comparison of the relative composition of the NPs before and after annealing.

Fe_3O_4 and Fe_2O_3 peaks are shifted toward higher energies compared to that of FeO. For the metallic Fe foil, the absorption energy is found to be ∼1.3 eV lower compared to divalent FeO (Supporting Information Figure S2). The shapes of the XANES profiles of Fe_3O_4 and γ-Fe_2O_3 are similar because they both have an inverse spinel crystal structure with a similar lattice constant. Differences are due to the fact that γ-Fe_2O_3 has cation vacancies at its octahedral sites. FeO has different bonding arrangements caused by the different crystallographic structure (rock salt structure). Therefore, they show distinctly different behavior in the XANES spectra. The half-maximum position of γ-Fe_2O_3 is 1.7 ± 0.3 eV higher compared to Fe_3O_4 and 3.2 ± 0.5 eV higher compared to FeO. Moreover, the peak position of the pre-edge is found at a slightly lower energy for the completely divalent Fe system FeO compared to the completely trivalent Fe system γ-Fe_2O_3. This will be discussed later in detail.

The XANES spectrum of the as-prepared iron oxide NPs shows a similar shape as that for Fe_3O_4 and γ-Fe_2O_3. This indicates that the particles have a mainly spinel structure. However, the half-maximum position for the NPs lies between that of the Fe_3O_4 and γ-Fe_2O_3. By fitting the XANES spectra of the NPs using a linear combination of the FeO, Fe_3O_4, and γ-Fe_2O_3 reference data, one can obtain the relative composition inside the particles. For the best fit, we use 2.5% weighted FeO, 44.9% Fe_3O_4, and 52.6% γ-Fe_2O_3 (Supporting Information Figure S3). However, even for the best fit, there are slight mismatches around the pre-edge and the maximum position of the spectrum. This is possibly due to the distorted structure at the interface between different phases or at the surface of the particles.

To study how the composition changes inside the NPs after oxidation, we compared the results obtained from the as-prepared sample with that of the particles after being oxidized in air at 50 °C for 24 h. As can be seen in Figure 2a, the spectrum shifts further toward higher energies after annealing and becomes more similar to the pure γ-Fe_2O_3 data. This indicates that the particles are transformed to mainly the γ-Fe_2O_3 phase, which matches the expectation such that thermal annealing in air should yield a transformation to mainly maghemite.[21] From a linear combination fit, we obtain that the annealed NPs are composed of 83.9 ± 5% γ-Fe_2O_3 and 16.1 ± 5% Fe_3O_4. Obviously, a significant increase of the γ-Fe_2O_3 fraction is found as expected. These results also agree with the conclusions of previous magnetometry studies on iron oxide NPs.[21]

Compared to the linear combination fit of the as-prepared sample, the fit of the XANES spectrum of the oxidized sample matches better with the experimental data (Supporting

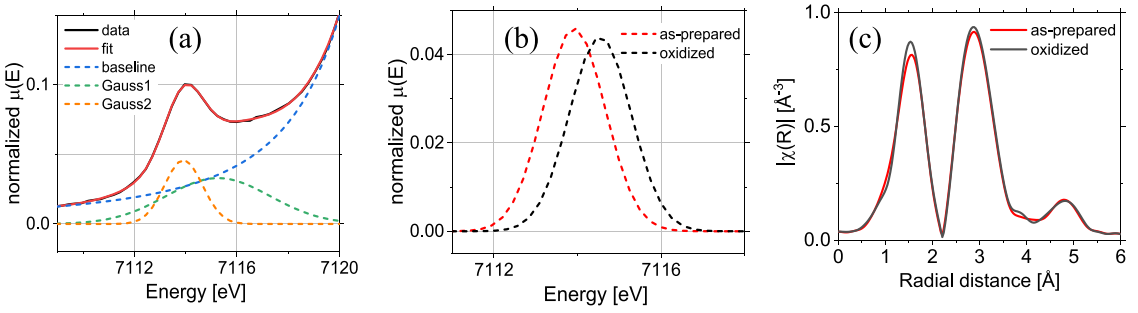

Figure 3. (a) Pre-edge spectrum of the as-prepared iron oxide NPs and the best model calculated using two Gaussian functions (using the Larch package). (b) Comparison of the (normalized and background-corrected) pre-edge spectra (Fe K-edge) of 14 nm iron oxide NPs before and after annealing. (c) Comparison of the Fourier transforms of the Fe K-edge EXAFS spectra of iron oxide NPs before and after annealing.

https://doi.org/10.1021/acs.jpcc.3c01023
J. Phys. Chem. C 2023, 127, 12077−12083

Information Figure S3). This indicates that there is less distortion inside the NPs compared to the bulk spinel structure than the as-prepared sample. This further confirms that the oxidized NPs tend to be single-phase γ-Fe_2O_3.

In Figure 2b, the ratios of different components inside the NPs are compared before and after annealing. The amount of FeO is negligibly small even in the as-prepared sample. The as-prepared particles are composed of an almost equal ratio of Fe_3O_4 and γ-Fe_2O_3. However, after annealing, the amount of γ-Fe_2O_3 significantly increased on the expense of the Fe_3O_4 phase.

In addition, the pre-edge features in the XANES spectra, which are related to the 1s to 3d electronic transitions of iron, provide valuable information about its oxidation state and the local coordination environment. The pre-edge feature of Fe-containing minerals are composed of two or more components depending on their oxidation state and the coordination number.[31,36,37,39−41] By analyzing the centroid position as well as the integrated area, one can estimate the ratio of Fe^{2+} to Fe^{3+}.

The pre-edge feature of both the as-prepared and the oxidized NPs can be fitted well with either two Gaussian or two pseudo-Voigt (50:50) functions. The peak position as well as the characteristics of different components obtained from both Gaussian and pseudo-Voigt functions are similar. Figure 3a shows the pre-edge spectrum of the as-prepared NPs compared with the best fit using two Gaussian functions. The component showing a peak at the lower energy (~7114 eV) arises from the mixture of Fe^{2+} and Fe^{3+}. However, the peak at about 7115 eV is not predicted in theory for the 1s to 3d transition. This peak is assigned to the hybridization of the 4p orbitals and oxygen. Therefore, the peak is excluded from analysis when estimating the redox ratio of the Fe^{2+} and Fe^{3+} mixtures. After background subtraction (including the baseline and the broad peak at ~7115 eV), the shape of the normalized pre-edge feature for both the as-prepared and the annealed particles is similar to that reported for γ-Fe_2O_3,[31] as can be seen in Figure 3b. However, the centroid of the peak shifts toward higher energy upon annealing. To obtain a quantitative analysis, the parameters extracted from the Gaussian fits are listed in Table 1. The centroid position for the as-prepared sample is found at 7113.920 eV, which is about 0.6 eV lower compared to that of the annealed NPs. The difference between the centroids for Fe^{2+} and Fe^{3+} was reported to be 1.5 eV.[31,39−41] Since both the as-prepared and annealed NPs are a mixture of Fe^{2+} and Fe^{3+} with different ratios, the spectra are an incoherent superposition of that of Fe^{2+} and Fe^{3+} with different ratios. Therefore, the difference in the centroid position is smaller compared to the one between pure Fe^{2+} and Fe^{3+}.

Table 1. Pre-Edge Characteristics of Iron Oxide NPs Fitted Using a Gaussian Function

		component	
sample	centroid (eV)	area	FWHM
as-prepared	7113.920(67)	0.0853(18)	1.744(21)
oxidized	7114.542(84)	0.0816(21)	1.737(26)

In previous publications,[31,39−41] the Fe K-edge is calibrated to 7111.08 eV. However, the Fe K-edge in this study is calibrated to 7112 eV using a piece of Fe foil. Therefore, the peak position obtained from this work is about 1 eV higher than the results shown in refs 31, 39, 41. Comparing the peak position and the integrated area of the component at lower energy with the literature results, the composition of the as-prepared NPs is estimated to be a mixture of 45% octahedrally coordinated Fe^{2+} and 55% Fe^{3+} at both the octahedral and tetrahedral sites. Assuming the particles are purely Fe_3O_4, the Fe^{2+} ratio is expected to be about 33%. However, the as-prepared NPs contain more than 33% Fe^{2+}. This means that there is a considerable amount of FeO in the samples. This result is in contradiction to the magnetometry and XANES results. The reason for this contradiction is that for this estimation, we assume that all Fe^{2+} at the octahedral sites are oxidized to octahedrally coordinated Fe^{3+}, as expected in bulk. However, at the nanometer scale, the coordination number is often reduced due to missing neighbors at the surface. This is confirmed by fitting the Fourier transformation of the EXAFS spectra (Supporting Information Figures S6 and S7). The coordination numbers obtained from the fittings are listed in Table S2 (Supporting Information). Moreover, the crystal structure might be distorted at the interface between different phases. Considering the missing oxygen around both the Fe^{2+} and Fe^{3+} ions, the Fe^{3+} content inside the NPs is estimated to be 50−80% for the as-prepared sample. After annealing, the Fe^{3+} ratio is estimated to be about 95%. These results agree with the values obtained from the linear combination.

Moreover, the bond lengths of Fe−O and Fe−Fe inside the NPs are obtained by fitting the Fourier transforms of the EXAFS spectra over a k-range of 2−12 $Å^{-1}$ (Supporting Information Figures S6 and S7). The Fe−O bond length is found to be 1.953 ± 0.005 Å. For Fe^O−Fe^O and Fe^O−Fe^T, the bond lengths are 2.984 ± 0.005 and 3.475 ± 0.005 Å, respectively, for the as-prepared sample. These values match the previously reported results for bulk γ-Fe_2O_3.[14] However, the coordination numbers are smaller compared to the theoretical values (Supporting Information Table S2). This is due to both the self-absorption and the finite size effect of the NPs, where interaction partners are missing at the surface. Compared to 1.5 μm size maghemite particles, which has a fraction of ~10^{-7} Fe at the surface, the Fe fraction at the surface of 15 nm NPs becomes ~5−10%. Therefore, the surface effect plays an important role on the properties in nano-scaled systems. Moreover, the finite size effect is more pronounced for the higher electron shells. Therefore, the difference between the fitted value and the literature value is greater for the higher shells. During oxidation, the Fe ions may migrate toward the surface of the particles and bond with the oxygen ions in air, as reported in the literature.[14] This migration could result in slight improvements in the crystallinity and size of the NPs. As can be seen in Figure 3c, the bond lengths do not show any obvious change before and after annealing. However, the coordination number of Fe−O increases slightly upon annealing.

4. CONCLUSIONS

In this work, we demonstrate that hard X-ray absorption spectroscopy combined with magnetometry is a powerful technique to perform characterizations on the composition of iron oxide NPs. ZFC/FC magnetization curves of the as-prepared iron oxide NPs show characteristic features indicating that the particles are a mixture of γ-Fe_2O_3 with a small ratio of Fe_3O_4. There is no clear indication of the existence of FeO. However, due to the possible overlapping of the bulk Néel temperature of FeO with the peak temperature of the NP

https://doi.org/10.1021/acs.jpcc.3c01023
J. Phys. Chem. C 2023, 127, 12077−12083

system or the suppression of the bulk Néel temperature due to the finite size effect, the existence of a small amount of FeO in the samples cannot be excluded. These results are further confirmed by the exchange bias effect found in the hysteresis loop of the as-prepared samples measured at 5 K. However, it is difficult to make an accurate estimation of the ratio of different compositions inside the NPs from the magnetometry results. Therefore, we performed hard X-ray absorption spectroscopy measurements at the Fe K-edge. By fitting the XANES spectra of the NPs using a linear combination of FeO, Fe_3O_4, and γ-Fe_2O_3 references, we obtain a composition of 2.5 ± 5% FeO, 44.9 ± 5% Fe_3O_4, and 52.6 ± 5% γ-Fe_2O_3 in the as-prepared sample. Upon thermal annealing, a significant amount of Fe_3O_4 is oxygenated to γ-Fe_2O_3 (44.9 to 83.9%). These results are further confirmed by analyzing the pre-edge spectra. The behavior of the pre-edge feature for both the as-prepared and the annealed NPs is comparable to literature results on γ-Fe_2O_3. Comparing their peak position and integrated intensity with the literature values, the Fe^{3+} ratio inside the particles is estimated to be 50−80% for the as-prepared NPs and 95% for the annealed NPs. These results agree with the values obtained from the linear combination of the XANES spectra. Furthermore, the Fe−O and Fe−Fe bond lengths obtained from the Fourier transform of the EXAFS spectra agree with the theoretical values. An increase in the coordination number is observed after the annealing procedure. These results provide valuable information for understanding the relationship between the structural composition of iron oxide NPs and their magnetic properties.

■ ASSOCIATED CONTENT

Supporting Information

The Supporting Information is available free of charge at https://pubs.acs.org/doi/10.1021/acs.jpcc.3c01023.

Synthesis of the iron oxide nanoparticles, high resolution TEM image and SAXS pattern of the iron oxide nanoparticles, XANES spectra of the Fe foil and iron oxide references, XANES spectra of the 14 nm iron oxide nanoparticles, pre-edge spectrum of the oxidized iron oxide nanoparticles, Fourier transform of the EXAFS spectra of the 14 nm iron oxide nanoparticles with fitting, and magnetometry results of the oxidized nanoparticles and tables with the results of the pre-edge fitting and the fitting results of the EXAFS spectra. (PDF)

■ AUTHOR INFORMATION

Corresponding Author

Xiao Sun − *Deutsches Elektronen-Synchrotron DESY, 22607 Hamburg, Germany;* orcid.org/0000-0001-5428-3526; Email: xiao.sun@desy.de

Authors

Akhil Tayal − *Deutsches Elektronen-Synchrotron DESY, 22607 Hamburg, Germany;* orcid.org/0000-0001-8152-4209

Aladin Ullrich − *Lehrstuhl für Experimentalphysik IV, Universität Augsburg, 86135 Augsburg, Germany*

Oleg Petracic − *Jülich Centre for Neutron Science JCNS and Peter Grünberg Institut PGI, JARA-FIT, Forschungszentrum Jülich GmbH, 52425 Jülich, Germany*

Sylvio Haas − *Deutsches Elektronen-Synchrotron DESY, 22607 Hamburg, Germany;* orcid.org/0000-0001-7066-0205

Complete contact information is available at: https://pubs.acs.org/10.1021/acs.jpcc.3c01023

Notes

The authors declare no competing financial interest.

■ ACKNOWLEDGMENTS

We would like to thank Chen Shen and Florian Bertram for their support of the SAXS measurement at the P08 beamline at PETRA III. We would also like to thank Edmund Welter and Morgane Desmau for their support with the XAS measurements at the P65 beamline at PETRA III. We further acknowledge Wolfgang Caliebe and Thomas Brückel for the fruitful discussion. DESY is supported by the German Ministry for Research and Education (BMBF) within the Helmholtz Association.

■ REFERENCES

(1) Reguera, J.; Jiménez de Aberasturi, D.; Henriksen-Lacey, M.; Langer, J.; Espinosa, A.; Szczupak, B.; Wilhelm, C.; Liz-Marzán, L. M. Janus Plasmonic−magnetic Gold−iron Oxide Nanoparticles as Contrast Agents for Multimodal Imaging. *Nanoscale* **2017**, *9*, 9467−9480.

(2) Rivas, J.; Bañobre-López, M.; Piñeiro-Redondo, Y.; Rivas, B.; López-Quintela, M. A. Magnetic Nanoparticles for Application in Cancer Therapy. *J. Magn. Magn. Mater.* **2012**, *324*, 3499−3502.

(3) Riedl, J. C.; Sarkar, M.; Fiuza, T.; Cousin, F.; Depeyrot, J.; Dubois, E.; Mériguet, G.; Perzynski, R.; Peyre, V. Design of Concentrated Colloidal Dispersions of Iron Oxide Nanoparticles in Ionic Liquids: Structure and Thermal Stability from 25 to 200 °C. *J. Colloid Interface Sci.* **2022**, *607*, 584−594.

(4) Demirelli, M.; Peyre, V.; Sirieix-Plénet, J.; Malikova, N.; Fresnais, J. Influence of Polycation/Cation Competition on the Aggregation Threshold of Magnetic Nanoparticles. *Colloids Surf., A* **2021**, *612*, No. 125876.

(5) Honecker, D.; Bersweiler, M.; Erokhin, S.; Berkov, D.; Chesnel, K.; Venero, D. A.; Qdemat, A.; Disch, S.; Jochum, J. K.; Michels, A.; Bender, P. Using Small-Angle Scattering to Guide Functional Magnetic Nanoparticle Design. *Nanoscale Adv.* **2022**, *4*, 1026−1059.

(6) Orozco-Henao, J. M.; Coral, D. F.; Muraca, D.; Moscoso-Londoño, O.; Mendoza Zélis, P.; Fernandez van Raap, M. B.; Sharma, S. K.; Pirota, K. R.; Knobel, M. Effects of Nanostructure and Dipolar Interactions on Magnetohyperthermia in Iron Oxide Nanoparticles. *J. Phys. Chem. C* **2016**, *120*, 12796−12809.

(7) Cooper, S. R.; Plummer, L. K.; Cosby, A. G.; Lenox, P.; Jander, A.; Dhagat, P.; Hutchison, J. E. Insights into the Magnetic Properties of Sub-10 nm Iron Oxide Nanocrystals through the Use of a Continuous Growth Synthesis. *Chem. Mater.* **2018**, *30*, 6053−6062.

(8) Efremova, M. V.; Spasova, M.; Heidelmann, M.; Grebennikov, I. S.; Li, Z.-A.; Garanina, A. S.; Tcareva, I. O.; Savchenko, A. G.; Farle, M.; Klyachko, N. L.; et al. Room Temperature Synthesized Solid Solution AuFe Nanoparticles and Their Transformation into Au/Fe Janus Nanocrystals. *Nanoscale* **2021**, *13*, 10402−10413.

(9) Ullrich, A.; Rahman, M. M.; Longo, P.; Horn, S. Synthesis and High-Resolution Structural and Chemical Analysis of Iron-Manganese-Oxide Core-Shell Nanocubes. *Sci. Rep.* **2019**, *9*, 19264.

(10) Ullrich, A.; Hohenberger, S.; Özden, A.; Horn, S. Synthesis of Iron Oxide/Manganese Oxide Composite Particles and Their Magnetic Properties. *J. Nanopart. Res.* **2014**, *16*, 2580.

(11) Köhler, T.; Feoktystov, A.; Petracic, O.; Kentzinger, E.; Bhatnagar-Schöffmann, T.; Feygenson, M.; Nandakumaran, N.; Landers, J.; Wende, H.; Cervellino, A.; et al. Mechanism of

Magnetization Reduction in Iron Oxide Nanoparticles. *Nanoscale* **2021**, *13*, 6965−6976.
(12) Soares, P. I. P.; Laia, C. A. T.; Carvalho, A.; Pereira, L. C. J.; Coutinho, J. T.; Ferreira, I. M. M.; Novo, C. M. M.; Borges, J. P. Iron Oxide Nanoparticles Stabilized with a Bilayer of Oleic Acid for Magnetic Hyperthermia and MRI Applications. *Appl. Surf. Sci.* **2016**, *383*, 240−247.
(13) Lappas, A.; Antonaropoulos, G.; Brintakis, K.; Vasilakaki, M.; Trohidou, K. N.; Iannotti, V.; Ausanio, G.; Kostopoulou, A.; Abeykoon, M.; Robinson, I. K.; Bozin, E. S. Vacancy-Driven Noncubic Local Structure and Magnetic Anisotropy Tailoring in Fe_xO-$Fe_{3-\delta}O_4$ Nanocrystals. *Phys. Rev. X* **2019**, *9*, No. 041044.
(14) Cornell, R. M.; Schwertmann, U. *The Iron Oxides: Structure, Properties, Reactions, Occurrences and Uses*; Wiley-VCH, 2003. doi: DOI: 10.1002/3527602097.
(15) Kugel, G. E.; Hennion, B.; Carabatos, C. Low-Energy Magnetic Excitations in Wustite ($Fe_{1-x}O$). *Phys. Rev. B* **1978**, *18*, 1317−1321.
(16) 1.1.3 Maghemite gamma-Fe2}2O3. In *The Landolt-Börnstein database*; Hellwege, K.-H., Ed.; Springer: Berlin, 1970; Vol. *4a*, pp. 8−16. doi: DOI: 10.1007/10201420_7.
(17) Roth, W. L. Defects in the Crystal and Magnetic Structures of Ferrous Oxide. *Acta Crystallogr.* **1960**, *13*, 140−149.
(18) Walz, F. The Verwey Transition - a Topical Review. *J. Phys.: Condens. Matter* **2002**, *14*, R285−R340.
(19) Verwey, E. J. W. Electronic Conduction of Magnetite (Fe_3O_4) and Its Transition Point at Low Temperatures. *Nature* **1939**, *144*, 327−328.
(20) García, J.; Subías, G. The Verwey Transition-a New Perspective. *J. Phys.: Condens. Matter* **2004**, *16*, R145−R178.
(21) Benitez, M. J.; Mishra, D.; Szary, P.; Badini Confalonieri, G. A.; Feyen, M.; Lu, A. H.; Agudo, L.; Eggeler, G.; Petracic, O.; Zabel, H. Structural and Magnetic Characterization of Self-Assembled Iron Oxide Nanoparticle Arrays. *J. Phys.: Condens. Matter* **2011**, *23*, No. 126003.
(22) Bedanta, S.; Barman, A.; Kleemann, W.; Petracic, O.; Seki, T. Magnetic Nanoparticles: A Subject for Both Fundamental Research and Applications. *J. Nanomater.* **2013**, *2013*, 1−22.
(23) Wang, L.-M.; Petracic, O.; Kentzinger, E.; Rücker, U.; Schmitz, M.; Wei, X.-K.; Heggen, M.; Brückel, T. Strain and Electric-Field Control of Magnetism in Supercrystalline Iron Oxide Nanoparticle-$BaTiO_3$ Composites. *Nanoscale* **2017**, *9*, 12957−12962.
(24) Fiorani, D.; Dormann, J. L.; Cherkaoui, R.; Tronc, E.; Lucari, F.; D'Orazio, F.; Spinu, L.; Nogues, M.; Garcia, A.; Testa, A. M. Collective Magnetic State in Nanoparticles Systems. *J. Magn. Magn. Mater.* **1999**, *196-197*, 143−147.
(25) Wetterskog, E.; Tai, C. W.; Grins, J.; Bergström, L.; Salazar-Alvarez, G. Anomalous Magnetic Properties of Nanoparticles Arising from Defect Structures: Topotaxial Oxidation of $Fe_{1-x}O|Fe_{3-\delta}O_4$ Corelshell Nanocubes to Single-Phase Particles. *ACS Nano* **2013**, *7*, 7132−7144.
(26) Disch, S.; Wetterskog, E.; Hermann, R. P.; Salazar-alvarez, G.; Busch, P.; Brückel, T.; Bergström, L.; Kamali, S. Shape Induced Symmetry in Self-Assembled Mesocrystals of Iron Oxide Nanocubes. *Nano Lett.* **2011**, *11*, 1651−1656.
(27) Anupama, A. V.; Keune, W.; Sahoo, B. Thermally Induced Phase Transformation in Multi-Phase Iron Oxide Nanoparticles on Vacuum Annealing. *J. Magn. Magn. Mater.* **2017**, *439*, 156−166.
(28) Kuzmin, A.; Chaboy, J. EXAFS and XANES Analysis of Oxides at the Nanoscale. *IUCrJ* **2014**, *1*, 571−589.
(29) Okudera, H.; Yoshiasa, A.; Murai, K. I.; Okube, M.; Takeda, T.; Kikkawa, S. Local Structure of Magnetite and Maghemite and Chemical Shift in Fe K-Edge XANES. *J. Mineral. Petrol. Sci.* **2012**, *107*, 127−132.
(30) Tayal, A.; Seo, O.; Kim, J.; Kusada, K.; Kitagawa, H.; Sakata, O. Investigation of Local Structure and Enhanced Thermal Stability of Ir-Doped PdRu Nanoparticles for Three-Way Catalytic Applications. *J. Phys. Chem. C* **2021**, *125*, 20583−20591.
(31) Wilke, M.; Farges, F.; Petit, P. E.; Brown, G. E., Jr.; Martin, F. Oxidation State and Coordination of Fe in Minerals: An Fe K-XANES Spectroscopic Study. *Am. Mineral.* **2001**, *86*, 714−730.
(32) Piquer, C.; Laguna-Marco, M. A.; Roca, A. G.; Boada, R.; Guglieri, C.; Chaboy, J. Fe K-Edge X-Ray Absorption Spectroscopy Study of Nanosized Nominal Magnetite. *J. Phys. Chem. C* **2014**, *118*, 1332−1346.
(33) Juhin, A.; Sainctavit, P.; Ollefs, K.; Sikora, M.; Filipponi, A.; Glatzel, P.; Wilhelm, F.; Rogalev, A. X-Ray Magnetic Circular Dichroism Measured at the Fe K-Edge with a Reduced Intrinsic Broadening: X-Ray Absorption Spectroscopy versus Resonant Inelastic x-Ray Scattering Measurements. *J. Phys.: Condens. Matter* **2016**, *28*, No. 505202.
(34) Rubio-Zuazo, J.; Chainani, A.; Taguchi, M.; Malterre, D.; Serrano, A.; Castro, G. R. Electronic Structure of FeO, γ-Fe_2O_3, and Fe_3O_4 Epitaxial Films Using High-Energy Spectroscopies. *Phys. Rev. B* **2018**, *97*, 1−9.
(35) Andersen, H. L.; Saura-Múzquiz, M.; Granados-Miralles, C.; Canévet, E.; Lock, N.; Christensen, M. Crystalline and Magnetic Structure-Property Relationship in Spinel Ferrite Nanoparticles. *Nanoscale* **2018**, *10*, 14902−14914.
(36) Caliebe, W. A.; Kao, C.-C.; Hastings, J. B.; Taguchi, M.; Kotani, A.; Uozumi, T.; de Groot, F. M. F. 1*s*2*p* Resonant Inelastic X-Ray Scattering in α-Fe_2O_3. *Phys. Rev. B* **1998**, *58*, 13452−13458.
(37) Petit, P. E.; Farges, F.; Wilke, M.; Solé, V. A. Determination of the Iron Oxidation State in Earth Materials Using XANES Pre-Edge Information. *J. Synchrotron Radiat.* **2001**, *8*, 952−954.
(38) Seema; Tayal, A.; Amir, S. M.; Pütter, S.; Mattauch, S.; Gupta, M. Structural, Electronic, and Magnetic Properties of Co_4N Thin Films Deposited Using HiPIMS. *J. Alloys Compd.* **2021**, *863*, No. 158052.
(39) Wilke, M.; Partzsch, G. M.; Bernhardt, R.; Lattard, D. Determination of the Iron Oxidation State in Basaltic Glasses Using XANES at the K-Edge. *Chem. Geol.* **2004**, *213*, 71−87.
(40) Wilke, M.; Partzsch, G. M.; Bernhardt, R.; Lattard, D. Determination of the Iron Oxidation State in Basaltic Glasses Using XANES at the K-Edge. *Chem. Geol.* **2005**, *220*, 143−161.
(41) Wilke, M.; Hahn, O.; Woodland, A. B.; Rickers, K. The Oxidation State of Iron Determined by Fe K-Edge XANES -Application to Iron Gall Ink in Historical Manuscripts. *J. Anal. At. Spectrom.* **2009**, *24*, 1364−1372.
(42) Park, J.; An, K.; Hwang, Y.; Park, J.-G.; Noh, H.-J.; Kim, J.-Y.; Park, J.-H.; Hwang, N.-M.; Hyeon, T. Ultra-Large-Scale Syntheses of Monodisperse Nanocrystals. *Nat. Mater.* **2004**, *3*, 891−895.
(43) Petracic, O.; Chen, X.; Bedanta, S.; Kleemann, W.; Sahoo, S.; Cardoso, S.; Freitas, P. P. Collective States of Interacting Ferromagnetic Nanoparticles. *J. Magn. Magn. Mater.* **2006**, *300*, 192−197.
(44) Wetterskog, E.; Klapper, A.; Disch, S.; Josten, E.; Hermann, R. P.; Rücker, U.; Brückel, T.; Bergström, L.; Salazar-Alvarez, G. Tuning the Structure and Habit of Iron Oxide Mesocrystals. *Nanoscale* **2016**, *8*, 15571−15580.
(45) Mishra, D.; Benitez, M. J.; Petracic, O.; Badini Confalonieri, G. A.; Szary, P.; Brüssing, F.; Theis-Bröhl, K.; Devishvili, A.; Vorobiev, A.; Konovalov, O.; et al. Self-Assembled Iron Oxide Nanoparticle Multilayer: X-Ray and Polarized Neutron Reflectivity. *Nanotechnology* **2012**, *23*, No. 055707.
(46) Mørup, S.; Hansen, M. F.; Frandsen, C. Magnetic Interactions between Nanoparticles. *Beilstein J. Nanotechnol.* **2010**, *1*, 182−190.
(47) Majetich, S. A.; Wen, T.; Thompson Mefford, O. Magnetic Nanoparticles. *MRS Bull.* **2013**, *38*, 899−903.
(48) Bedanta, S.; Petracic, O.; Kleemann, W. Supermagnetism. In *Handbook of Magnetic Materials, Vol.23*; Buschow, K. J. H., Ed.; Elsevier, 2015.
(49) Ebbing, A.; Hellwig, O.; Agudo, L.; Eggeler, G.; Petracic, O. Tuning the Magnetic Properties of Co Nanoparticles by Pt Capping. *Phys. Rev. B* **2011**, *84*, No. 012405.
(50) Shevchenko, E. V.; Bodnarchuk, M. I.; Kovalenko, M. V.; Talapin, D. V.; Smith, R. K.; Aloni, S.; Heiss, W.; Alivisatos, A. P.

Gold/Iron Oxide Core/Hollow-Shell Nanoparticles. *Adv. Mater.* **2008**, *20*, 4323−4329.
(51) Chen, X.; Bedanta, S.; Petracic, O.; Kleemann, W.; Sahoo, S.; Cardoso, S.; Freitas, P. P. Superparamagnetism versus Superspin Glass Behavior in Dilute Magnetic Nanoparticle Systems. *Phys. Rev. B* **2005**, *72*, No. 214436.
(52) Nogués, J.; Schuller, I. K. Exchange Bias. *J. Magn. Magn. Mater.* **1999**, *192*, 203−232.
(53) Nogués, J.; Sort, J.; Langlais, V.; Skumryev, V.; Suriñach, S.; Muñoz, J. S.; Baró, M. D. Exchange Bias in Nanostructures. *Phys. Rep.* **2005**, *422*, 65−117.
(54) Estrader, M.; López-Ortega, A.; Estradé, S.; Golosovsky, I. V.; Salazar-Alvarez, G.; Vasilakaki, M.; Trohidou, K. N.; Varela, M.; Stanley, D. C.; Sinko, M.; et al. Robust Antiferromagnetic Coupling in Hard-Soft Bi-Magnetic Core/Shell Nanoparticles. *Nat. Commun.* **2013**, *4*, 2960.
(55) Kiwi, M. Exchange Bias Theory. *J. Magn. Magn. Mater.* **2001**, *234*, 584−595.
(56) Mishra, S. K.; Radu, F.; Dürr, H. A.; Eberhardt, W. Training-Induced Positive Exchange Bias in NiFe/IrMn Bilayers. *Phys. Rev. Lett.* **2009**, *102*, No. 177208.
(57) Sun, X.; Klapper, A.; Su, Y.; Nemkovski, K.; Wildes, A.; Bauer, H.; Köhler, O.; Schilmann, A.; Tremel, W.; Petracic, O.; Brückel, T. Magnetism of Monomer MnO and Heterodimer FePt@MnO Nanoparticles. *Phys. Rev. B* **2017**, *95*, No. 134427.
(58) Trohidou, K. N.; Vasilakaki, M.; Del Bianco, L.; Fiorani, D.; Testa, A. M. Exchange Bias in a Magnetic Ordered/Disordered Nanoparticle System: A Monte Carlo Simulation Study. *J. Magn. Magn. Mater.* **2007**, *316*, e82−e85.
(59) Del Bianco, L.; Fiorani, D.; Testa, A. M.; Bonetti, E.; Signorini, L. Field-Cooling Dependence of Exchange Bias in a Granular System of Fe Nanoparticles Embedded in an Fe Oxide Matrix. *Phys. Rev. B* **2004**, *70*, No. 052401.
(60) Skumryev, V.; Stoyanov, S.; Zhang, Y.; Hadjipanayis, G.; Givord, D.; Nogués, J. Beating the Superparamagnetic Limit with Exchange Bias. *Nature* **2003**, *423*, 850−853.
(61) Sun, X.; Frey Huls, N.; Sigdel, A.; Sun, S. Tuning Exchange Bias in Core/Shell FeO/Fe_3O_4 Nanoparticles. *Nano Lett.* **2012**, *12*, 246−251.
(62) Ong, Q. K.; Wei, A.; Lin, X. M. Exchange Bias in Fe/Fe_3O_4 Core-Shell Magnetic Nanoparticles Mediated by Frozen Interfacial Spins. *Phys. Rev. B* **2009**, *80*, 1−6.
(63) Corrias, A.; Ennas, G.; Mountjoy, G.; Paschina, G. An X-Ray Absorption Spectroscopy Study of the Fe K Edge in Nanosized Maghemite and in Fe_2O_3-SiO_2 Nanocomposites. *Phys. Chem. Chem. Phys.* **2000**, *2*, 1045−1050.
(64) Jia, Y.; Huang, R.; Qi, R. Iron Single Atoms Anchored on Carbon Matrix/g-C_3N_4 Hybrid Supports by Single-Atom Migration-Trapping Based on MOF Pyrolysis. *Nanomaterials* **2022**, *12*, 1416.
(65) Chen, W. T.; Hsu, C. W.; Lee, J. F.; Pao, C. W.; Hsu, I. J. Theoretical Analysis of Fe K-Edge XANES on Iron Pentacarbonyl. *ACS Omega* **2020**, *5*, 4991−5000.
(66) Yuan, K.; Lützenkirchen-Hecht, D.; Li, L.; Shuai, L.; Li, Y.; Cao, R.; Qiu, M.; Zhuang, X.; Leung, M. K. H.; Chen, Y.; et al. Boosting Oxygen Reduction of Single Iron Active Sites via Geometric and Electronic Engineering: Nitrogen and Phosphorus Dual Coordination. *J. Am. Chem. Soc.* **2020**, *142*, 2404−2412.
(67) Ma, W.; Mao, J.; Yang, X.; Pan, C.; Chen, W.; Wang, M.; Yu, P.; Mao, L.; Li, Y. A Single-Atom Fe-N_4 Catalytic Site Mimicking Bifunctional Antioxidative Enzymes for Oxidative Stress Cytoprotection. *Chem. Commun.* **2019**, *55*, 159−162.

https://doi.org/10.1021/acs.jpcc.3c01023
J. Phys. Chem. C 2023, 127, 12077−12083